ORGANIC CHEMISTRY

Pyrgos[*n*]cages: Redefining antibacterial strategy against drug resistance

Yi Zhang[1]†, Miaomiao Luo[1]†, Xiangling Shi[1], Aimin Li[1], Wei Zhou[1], Yuyao Yin[2], Hui Wang[2], Wing-Leung Wong[3], Xinxin Feng[1]*, Qing He[1]*

Amid rising antibiotic resistance, the quest for advanced antibacterial agents to surpass microbial adaptation is paramount. This study introduces Pyrgos[*n*]cages (*n* = 1 to 4), pioneering multidecker cationic covalent organic cages engineered to combat drug-resistant bacteria via a dual-targeting approach. Synthesized through successive photocatalytic bromination and cage-forming reactions, these architectures stand out for their dense positive charge distribution, exceptional stability, and substantial rigidity. Pyrgos[*n*]cages exhibit potent bactericidal activity by disrupting bacterial membrane potential and binding to DNA. Notably, these structures show unparalleled success in eradicating both extracellular and intracellular drug-resistant pathogens in diverse infection scenarios, with antibacterial efficiency markedly increasing over 100-fold as the decker number rises from 1 to 3. This study provides an advance in antibacterial tactics and underscores the transformative potential of covalent organic cages in devising enduring countermeasures against antibiotic-resistant microbial threats.

INTRODUCTION

The rising tide of antibiotic-resistant bacteria poses a formidable threat to global health (*1*, *2*). The dwindling effectiveness of conventional antibiotics against these resistant strains heralds an urgent antibiotic crisis, necessitating a swift and comprehensive search for new antimicrobial methods (*3*–*5*). Among these, the discovery of unique chemical scaffolds with innovative bactericidal actions is crucial (*6*–*8*). In antibiotic research, targeting a singular enzyme often spurs resistance, as even minor changes in the drug target can lead to inefficacy (*9*–*11*). Monotherapeutic antibiotics that maintain effectiveness tend to target multiple enzymes or disrupt bacterial cell membranes (*12*, *13*). Consequently, the development of membrane-targeting antimicrobials is increasingly vital, given their resilience against evolutionary resistance mechanisms in bacteria (*13*, *14*). Research in this domain, inspired by natural membrane-targeting agents such as antimicrobial peptides (AMPs) and proteins, has spurred the synthesis of mimics aimed at combating multidrug-resistant bacterial infections (*15*–*17*). Cationic and hydrophobic attributes are essential for the effectiveness of cationic AMPs in antimicrobial activities (*18*). Typically, these AMPs manifest as cationic and amphipathic α-helical peptides, targeting anionic bacterial membranes (*18*, *19*). Their primary mechanism involves membrane penetration, leading to pore formation and subsequent bacterial membrane disruption, thereby combating multidrug-resistant bacteria effectively (*20*). However, the efficacy of AMPs and their analogs is challenged in animal systems, wherein high concentrations of salts and proteases can adversely affect their structural integrity and function (*21*).

To overcome these challenges, in addition to existing inorganic nanoparticles and inorganic/organic hybrid materials, various strategies have been investigated. These include modifying polypeptide structures, physically encapsulating polypeptides, and integrating multiple modification techniques (*21*–*24*). Alternatively, supramolecular macrocycles (e.g., cucurbiturils, cyclodextrins, calixarenes, and pillararenes) have risen over the past decades as promising molecular scaffolds for AMP mimics because of their facile synthesis, unique structures, adaptable functionalities, unusual host-guest complexation abilities, and dynamic modularity (*25*–*30*). More often than not, these macrocycles serve as ideal platforms for further functionalization antibacterial features, such as positive charges, through covalent or noncovalent interactions, presenting promising biological activity (*31*–*33*). For instance, in 2016, Zhang and co-workers (*34*) crafted a polypseudorotaxane by threading cucurbit[7]uril onto the lysine units of ε-poly-L-lysine hydrochlorides via host-guest complexation for effectively treating antibiotic-resistant infections. Later in 2019, Gao's group (*35*) designed a multifunctional zwitterionic pillar[5]arene that forms nanoaggregates with antibacterial properties against *Escherichia coli* and *Staphylococcus aureus* and effectively disrupts established *E. coli* biofilms, showing promise in overcoming bacterial resistance. In 2022, Guo's group (*36*) developed a hypoxia-responsive carrier, lactose-modified azocalix[4]arene, for targeted biofilm inhibition and enhanced antibacterial efficacy in diabetic wounds. Collectively, impressive are these recent advances in terms of the low cytotoxicity and relatively high antimicrobial activity of the supramolecular antibacterial agents. Although macrocycle-based antibacterial agents offer a promising solution to the challenges faced by AMPs, most, if not all, of them have been reported to predominantly kill extracellular bacteria through mechanisms such as disrupting bacterial membrane structure and function. Moreover, among them, it is exceedingly rare to encounter systems that effectively thwart the development of bacterial resistance evolution. Hence, ongoing search for new molecular scaffolds targeting intracellular drug-resistant bacteria is highly needed.

Structurally, AMPs, their synthetic analogs, and supramolecular macrocycle–based agents feature a relatively flexible architecture, characterized by variable and sparse charge distribution (*37*). This flexibility arises from the use of pliable linkages in attaching

[1]State Key Laboratory of Chemo/Biosensing and Chemometrics, College of Chemistry and Chemical Engineering, Hunan University, Changsha 410082, China. [2]Department of Clinical Laboratory, Peking University People's Hospital, Beijing 100044, China. [3]State Key Laboratory of Chemical Biology and Drug Discovery, Department of Applied Biology and Chemical Technology, The Hong Kong Polytechnic University, Hung Hom, Kowloon, Hong Kong SAR 999077, China.
*Corresponding author. Email: heqing85@hnu.edu.cn (Q.H.); xinxin_feng@hnu.edu.cn (X.F.)
†These authors contributed equally to this work.

functionalities to macrocyclic frameworks or from flexible polymer backbones for host-guest binding to the macrocycles (Fig. 1A). However, functionalized constructs with high rigidity and uniformly distributed charges at fixed positions remain unmet challenges, which could result in the discovery of conceptionally new antimicrobial agents for drug-resistant bacteria. Covalent organic cages have garnered increasing interest from the chemical community and beyond due to their tailored synthesis, ideal functionalization platforms, and unique binding pockets comparable to enzyme-binding sites, as well as their broad applications in molecular recognition, mass transport, gas separation, catalysis, and many others (*38*). In this contribution, we designed and synthesized a series of multidecker covalent organic cages, named Pyrgos[*n*] cages (with "Pyrgos" denoting a Greek tower and "*n*" indicating the number of deckers). Each level of these Pyrgos[*n*]cages is formed by two parallel benzene rings acting as the top and bottom and three positively charged imidazolium groups serving as the "walls" (Fig. 1B). Unprecedentedly, these functionalized molecules feature exceptionally high rigidity and up to 12 positive charges uniformly displaced at fixed positions. Consequently, the Pyrgos[*n*]cage series, synthesized through iterative photocatalytic bromination and cage-forming reactions, exhibited both strong bactericidal properties and biocompatibility. Their efficacy is rooted in a dual-action mechanism: disrupting bacterial membrane potential and binding to DNA (Fig. 1C). These structures proved highly effective across various bacterial infection models, successfully targeting not only extracellular but also intracellular bacteria in mammalian cells and mouse models. This underscores their potential as powerful, low-toxicity covalent organic cage–based agents against resistant infections, offering insights for future antimicrobial development.

RESULTS

Design and synthesis of Pyrgos[*n*]cages

In continuance of our efforts to develop new functional molecular systems via enclosing conventional cages to form carcerands and the like (e.g., superphanes) (*39*–*42*), we have conceived a new class of molecular constructs through axially stacking molecular cages in a vertical sequence. These structures, reminiscent of the Greek tower Pyrgos, can be suitably named "Pyrgos[*n*]cage," with *n* denoting the count of stacked deckers. The design is straightforward, but the synthesis is full of hardships. To achieve this goal, we selected benzene rings as the top and bottom and chose imidazolium as the connecting bridges based on their synthetic accessibility, rigidity, symmetry, charge distribution, and potential antimicrobial activity.

As shown in Fig. 2, the synthesis began with the easily prepared 1,3,5-tris(bromomethyl)benzene (**1b**), which was coupled with imidazole or benzimidazole using NaH in dimethylformamide (DMF) at room temperature to produce **2a** or **2b**, respectively. Subsequently, **2a** was reacted with **1a** or **1b** in CH_3CN under reflux for 48 hours, yielding asymmetrical Pyrgos[1]cage (**3**) with a 71% yield and symmetrical Pyrgos[1]cage (**P-1**) with an 84% yield. Notably, all three or six methyl groups on compounds **3** or **P-1** could be converted into bromomethyl units through photocatalytic bromination under ultraviolet light (360 nm, 100 W) in the presence of *N*-bromosuccinimide (NBS). This transformation follows the complete anion exchange of **3** and **P-1** with hexafluorophosphate (PF_6^-), resulting in the key intermediates **4a** (95% yield) and **4b** (83% yield). Moving forward, upon subjecting asymmetrical Pyrgos[1]cage, **4a** bearing three bromomethyl groups to cage-forming reaction with **2a** in CH_3CN under reflux for 48 hours led to the formation of expected asymmetrical Pyrgos[2]cage (**P-2a**) with a yield of 19%. Likewise, when **4b** was used to react with **2a** under typical

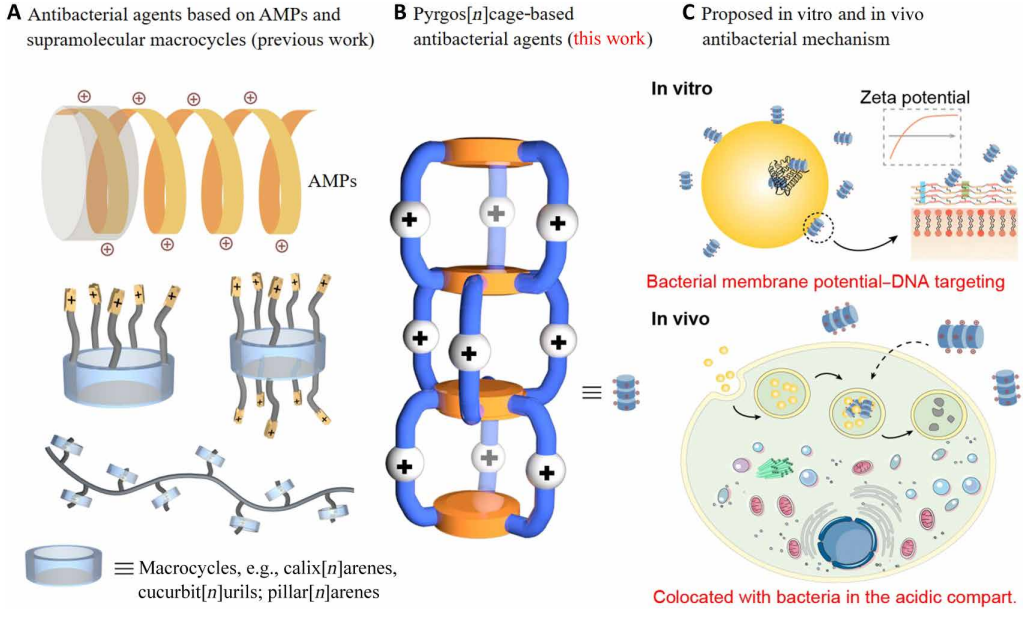

Fig. 1. Illustrative structures of the conventional and new antibacterial agents and the working mechanism of the latter. (**A**) AMP and supramolecular macrocycle–based antibacterial agents (previous work) and (**B**) Pyrgos[*n*]cage-based antibacterial agents (this work). (**C**) A proposed mechanism of Pyrgos[*n*]cages for killing in vitro and in vivo *S. aureus*.

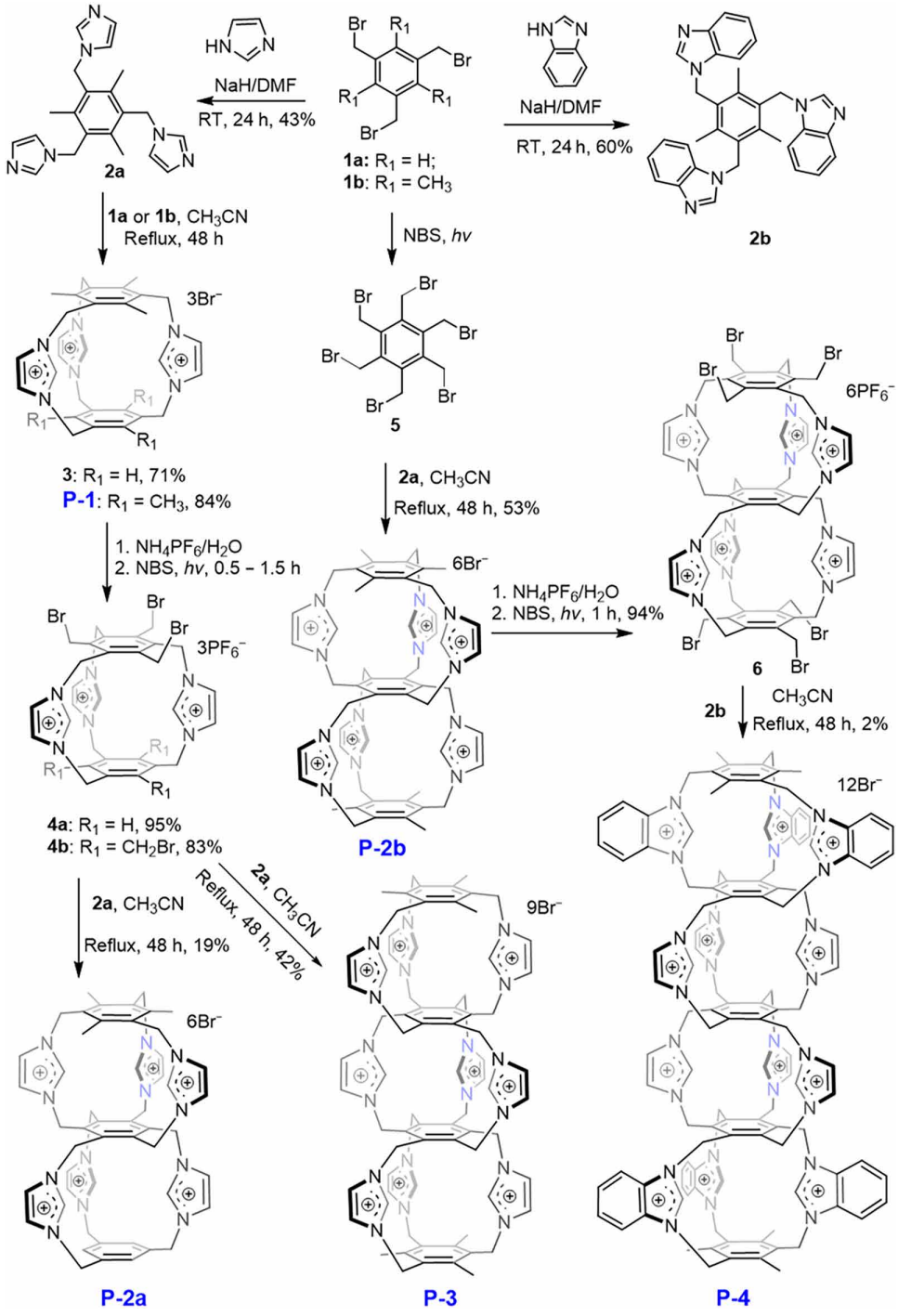

Fig. 2. Synthesis of Pyrgos[1]cage (P-1), Pyrgos[2]cages (P-2a and P-2b), Pyrgos[3]cage (P-3), and Pyrgos[4]cage (P-4). RT, room temperature.

cage-forming conditions, an unprecedented triple-decker Pyrgos[3]cage (**P-3**) was obtained, achieving a yield of 42%.

Advancing our synthesis further, when hexakis(bromomethyl) benzene (**5**), efficiently derived from **1b** through photocatalytic bromination with NBS, was treated with **2a** in acetonitrile under reflux for 48 hours, a symmetrical Pyrgos[2]cage (**P-2b**) was successfully produced in a yield of 53%. Much to our delight, **P-2b** was found able to be converted into its hexabromo-substituted variant (**6**) as white solid with a high efficiency of 95% yield, following complete anion exchange with PF_6^- and subsequent NBS-involved photocatalytic bromination. Eventually, an unusual tetradecker cage, Pyrgos[4]cage (**P-4**), was successfully obtained. This was achieved by reacting the key precursor **6** with **2b**, derived from the reaction of **1b** with benzimidazole in DMF using NaH as the base at room temperature for 24 hours, yielding 60%. Under typical cage-forming conditions, the final product was obtained in a 2% yield. Note that these

Pyrgos[*n*]cages were simply purified by precipitation or repeated recrystallization in acetonitrile, rather than normal chromatography. All Pyrgos[*n*]cages and the related key intermediates were fully characterized by standard spectroscopic analyses (see figs. S1 to S35).

X-ray single-crystal structures of Pyrgos[*n*]cages

We next performed crystallographic analysis to further support the formation of Pyrgos[*n*]cages (**P-2b**, **P-3**, and **P-4**). Specifically, a high-quality single crystal was obtained by slow diffusion of ethyl ether into a solution of **P-2b** in acetonitrile, after anion exchange with PF_6^-. The resulting crystal structure revealed that an expected double-decker molecular construct with two imidazolium-based covalent organic cages axially fused (Fig. 3, A and B). Each Pyrgos[2]cage molecule (**P-2b**) displayed a rigid and column-shaped conformation with three hexakis(methyl)benzenes in a face-to-face arrangement, forming two distinct deckers. Six imidazolium units evenly distributed between the each two adjacent parallel benzene rings contribute to the molecule's height of ~10.2 Å and a decker height of 5.1 Å (Fig. 3B and fig. S36). Although **P-2b** comprises two subcavities, they primarily exclude anions except fluoride due to the limited internal space being occupied by three hydrogen atoms from the imidazolium moieties (fig. S37). In addition, six counter PF_6^- anions in each unit cell indicated that Pyrgos[2]cage **P-2b** indeed carries six positive charges, as anticipated. These charges are uniformly distributed throughout the molecule, with each imidazolium unit contributing one positive charge (fig. S38).

In the case of Pyrgos[3]cage (**P-3**), single crystals suitable for x-ray crystallography were obtained by slowly evaporating a solution of **P-3** in water, again, after anion replacement with PF_6^-. The yielding crystal structure gave a triple-decker Pyrgos[3]cage, an axially expanded version of **P-2b** (Fig. 3, C and D, and figs. S39 and S40). This rigid molecular scaffold has a height of 15.8 Å with an averaged decker height of 5.3 Å. Within the unit cell, each **P-3** molecule is associated with about two bromides and seven PF_6^- as the counter anions, indicating that **P-3** carries nine evenly distributed positive charges across its nine imidazolium units (fig. S41). In a similar manner to the crystal growth of **P-3**, good-quality single crystals of Pyrgos[4]cage (**P-4**) were obtained through slow evaporation of a solution of **P-4** in a mixture of acetonitrile and water. The crystal structure of **P-4** showcased a remarkable tetradecker arrangement, featuring four perpendicularly stacked (benz)imidazolium-based cages (Fig. 3E). Impressively, the overall height of **P-4** was estimated to be ~21.1 Å, with decker heights measuring 5.2 Å for the benzimidazolium layers and 5.4 Å for the imidazolium levels (Fig. 3E and figs. S42 to S44). Notably, the structure exhibited a uniform distribution of 12 positive charges across its (benz)imidazolium units, as evidenced by the surrounding 12 bromide counter anions for each **P-4** molecule (figs. S42 and S45A). Compared to other Pyrgos[*n*]cage, Pyrgos[4]cage displays stronger symmetry. The H atoms in the (benz)imidazolium-based cavity and imidazolium-based cavity assemble two perfect equilateral triangle structure where side lengths were 3.0 and 4.2 Å, respectively (fig. S44). The excellent symmetry indicates that the rotation angles of imidazolium units in the same cavity are all the same. This unique symmetry brings extraordinary rigidity and stability to Pyrgos[4]cage. Taken in concert, these observations led us to conclude that a series of conceptionally new Pyrgos[*n*]cages, featuring straightforward synthesis, robust stability, pronounced rigidity, and densely packed positive charges, have been successfully established.

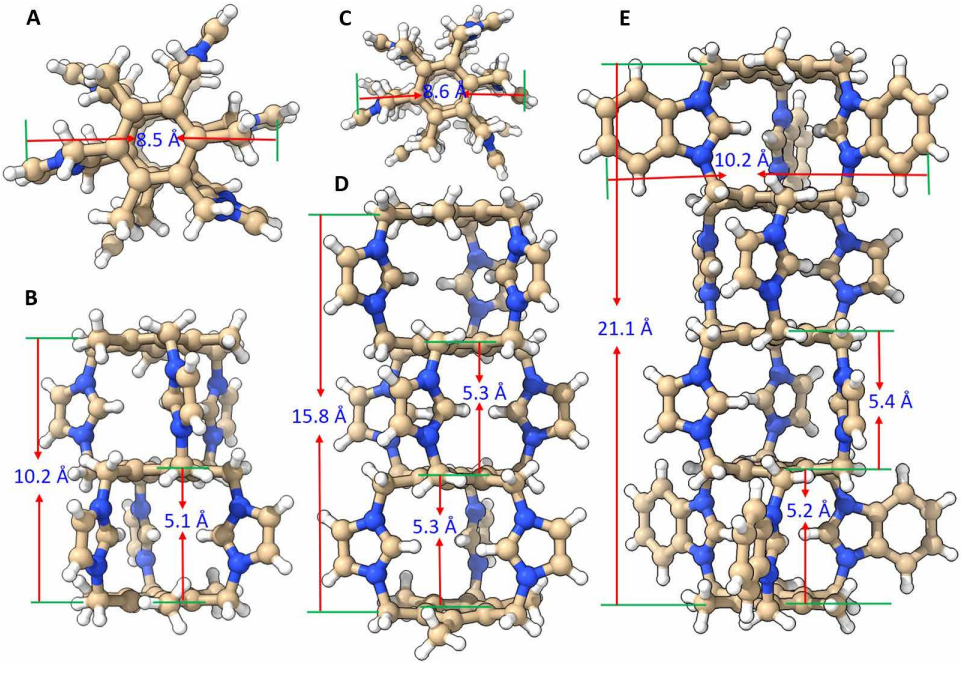

Fig. 3. Single-crystal x-ray structures of Pyrgos[*n*]cages. (**A**) Top view and (**B**) front view of **P-2b**. (**C**) Top view and (**D**) front view of **P-3**. (**E**) Front view of **P-4**. C, yellow; N, blue; H, white. Solvent molecules and counter anions are omitted for clarity. CCDC (Cambridge Crystallographic Data Center) P-2b: 2272285, P-3: 2270664, and P-4: 2270662 contain the supplementary crystallographic data for this paper. These data can be obtained free of charge via www.ccdc.cam.ac.uk/data_request/cif, by emailing data_request@ccdc.cam.ac.uk, or by contacting The CCDC, 12 Union Road, Cambridge CB2 1EZ, UK; fax: +441223 336033.

Antimicrobial activity of Pyrgos[*n*]cages with a suppression of resistance development

AMPs are characterized by their short length, relative flexibility, cationic nature, and amphipathic structure, offering broad-spectrum effectiveness against pathogens and rapid action, yet they face limitations such as potential toxicity to host cells and, inter alia, susceptibility to protease degradation (*21*). Thus, there is a compelling need for innovative molecular systems that can retain the benefits of AMPs while circumventing their limitations. In this context, Pyrgos[*n*]cages could be promising and potent antibacterial agents, owing to their special functionalities including (i) dense positive charge distribution, facilitating interactions with negatively charged bacterial membranes or DNA; (ii) rigid, metabolically resistant structure; and (iii) balanced hydrophobicity and hydrophilicity, reminiscent of classic supramolecular antibacterial agents.

To test our hypothesis, we next sought to evaluate the antibacterial activity and selectivity of these Pyrgos[*n*]cages against important clinical bacterial pathogens. *S. aureus* continues to pose a substantial threat to human health, resulting in high mortality rates attributed to severe systemic infections. This pathogen has acquired a reputation for its multidrug resistance capabilities, which, when combined with its extensive array of virulence factors exacerbating illnesses, renders it an exceedingly challenging organism to manage within clinical settings (*43*).The results were shown in Fig. 4A, table S1, and fig. S46. As expected, all Pyrgos[*n*]cages tested showed excellent antibacterial effects against *S. aureus*, methicillin-resistant *S. aureus* (MRSA), and other clinical multidrug-resistant clinical *S. aureus*, except for **P-4**, possibly hindered by its poor water (or dimethyl sulfoxide) solubility. Increasing the number of deckers in the Pyrgos[*n*]cages enhanced their effectiveness against Gram-positive bacteria. In sharp contrast, Pyrgos[*n*]cages exhibited nearly no antibacterial effect on Gram-negative bacteria, likely due to their uniquely dense outer membrane with lipopolysaccharides and divalent cations, which prevent Pyrgos[*n*]cages from entering (fig. S46B). We speculated that this could be attributed to the increase in cationicity and hydrophobicity of Pyrgos[*n*]cages, factors known to boost the antibacterial activity (*44*). Notably, **P-2b** and **P-3** demonstrated rapid antimicrobial kinetics, eradicating all *S. aureus* within an hour (fig. S47).

Pyrgos[*n*]cages demonstrate superior efficacy against clinical multidrug–resistant bacterial cells, surpassing most conventional antibiotics. This supports our hypothesis that Pyrgos[*n*]cages could operate through an unconventional antibacterial mechanism, enabling them to overcome common resistance determinants and maintain

A

μg/ml	P-1	P-2b	P-2a	P-3	P-4
S. aureus	4	1	0.725	0.188	N.D.
sklx001913a	2	0.125	0.125	<0.0325	N.D.
sklx001915a	4	0.125	<0.0325	<0.0325	N.D.
USA300	2	0.25	0.00625	<0.0325	N.D.
MRSA	1	0.25	0.25	0.125	N.D.
B.subtilis	1	0.25	0.25	0.125	N.D.
5-30	4	4	1	0.065	N.D.
1-71	4	2	0.5	<0.0325	N.D.
cfn464	16	4	1	0.25	N.D.
1-230	8	4	1	0.25	N.D.
cfn420	8	4	1	0.25	N.D.
cfn87	16	2	2	0.5	N.D.
6-31	16	6	3	0.25	N.D.
5-30	4	2	1	0.125	N.D.
5-2	8	4	1.5	0.125	N.D.
6-66	2	1	1	<0.0325	N.D.

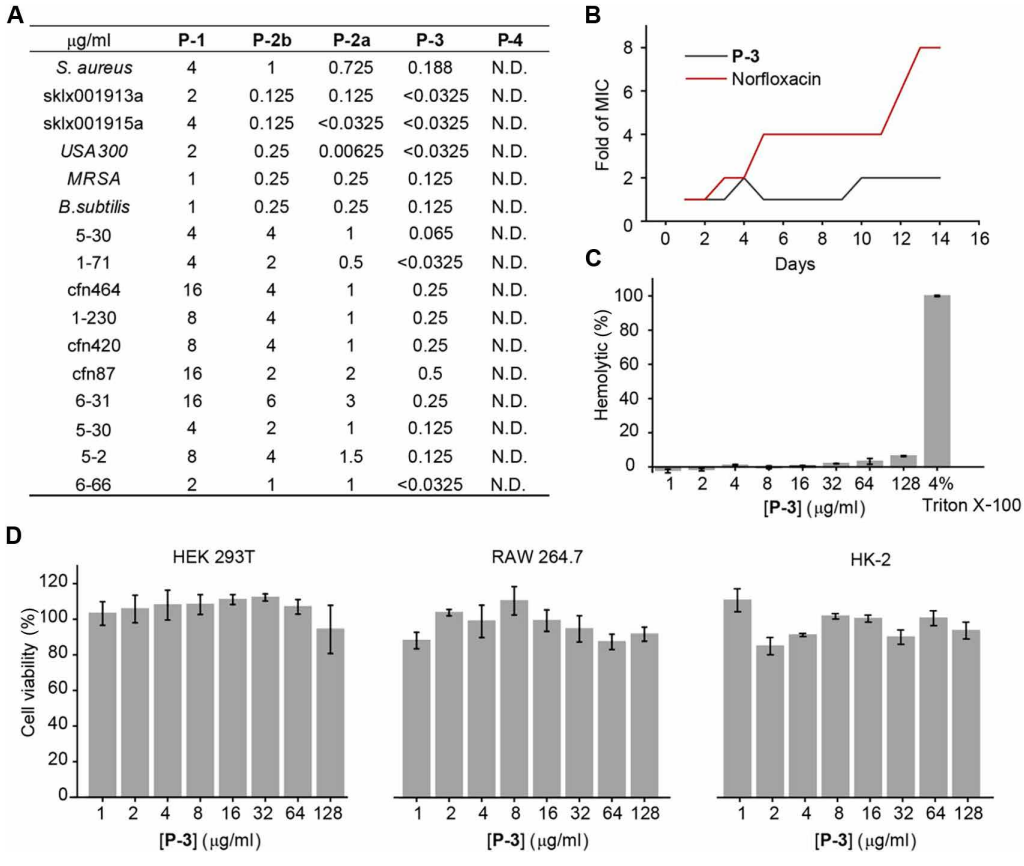

Fig. 4. Antimicrobial activity assays with Pyrgos[*n*]cages. (**A**) Minimum inhibitory concentration (MIC) values of Pyrgos[*n*]cages. Different strains, including laboratory strains and clinical isolates with multidrug resistance, were covered in the evaluation. sklx001913a, sklx001915a, 5-30, 1-7, cfn464, 1-230, cfn420, cfn87, 6-31, 5-30, 5-2, and 6-66 are *S. aureus* clinical isolates with multidrug resistance; MRSA and USA300 are methicillin-resistant *S. aureus* strains. *B. subtilis*, *Bacillus subtilis*; N.D., not determined. (**B**) Resistance evolution profile of *S. aureus* against **P-3** and norfloxacin. Norfloxacin exhibited a sharp increase in MIC by eightfold after 14 days. (**C**) Hemolytic activity of **P-3** with concentrations ranging from 1 to 128 μg/ml. (**D**) Cell viability assays of **P-3** on two mammalian cell lines (murine macrophage RAW 264.7, *H. sapiens* embryonic kidney cell line HEK 293T, and a human kidney cell line HK–2).

resistance resilience even under continuous drug pressure (Fig. 4B). In contrast to traditional antibiotics such as norfloxacin, which exhibited an eightfold increase in minimum inhibitory concentrations (MICs) during stepwise resistance evolution, Pyrgos[*n*]cages effectively limit the MIC change to twofold. These results suggested that the intracellular aggregation of Pyrgos[*n*]cages may suppress major resistance mechanisms.

In addition, note that Pyrgos[*n*]cages exhibited low eukaryotic cytotoxicity, as evidenced by hemolytic assays (Fig. 4C and fig. S48) and mammalian cell growth inhibition assays (Fig. 4D and fig. S49). These findings suggest that the mechanism of action of Pyrgos[*n*]cages may be specific to bacterial cells, a crucial characteristic for their consideration as antimicrobial agents.

Molecular insights into Pyrgos[*n*]cages: Dual targeting of membranes and DNA

Given the promising therapeutic index as observed above, we next sought to conduct an in-depth mechanistic investigation of Pyrgos[*n*]cages. Since Pyrgos[*n*]cages feature multiple and evenly distributed cationic sites, these could facilitate their interaction with negatively charged biomacromolecules, such as bacterial membranes and DNA. Thus, we first investigated the interaction between Pyrgos[*n*]cages and bacterial membrane, the outmost barrier of the cell envelope, through a comprehensive set of biochemical and microbiological assays. Membrane interaction was first studied by lipid interference assays with PG (phosphatidylglycerol; major membrane lipid of the bacteria). Our findings indicated that the antimicrobial activity of Pyrgos[*n*]cages could be suppressed by the addition of PG (Fig. 5A), with the greatest effect (8-fold MIC change) for **P-3** as compared to the shorter Pyrgos[*n*]cages (1.25- to 1.5-fold MIC changes). This result preliminary suggested that Pyrgos[*n*]cages showed affinity toward membrane lipid possibly via electrostatic interactions, which may lead to attachment of Pyrgos[*n*]cages on the surface of bacterial cells and alternation of the cell functions. To verify this hypothesis, we next measured the surface potential of *S. aureus* cells in the presence of Pyrgos[*n*]cages. As shown in Fig. 5B, in the absence of Pyrgos[*n*]cages, the zeta potential of *S. aureus* cells was largely negative because of the presence of anionic lipids including cardiolipin, PG, phosphatidylinositol, and teichoic acids as major components of its phospholipid lipid bilayer. With increasing concentration of cationic Pyrgos[*n*]cages (16 or 32 μg/ml), we found changes in the zeta potential of *S. aureus* from negative to positive. The results may indicate that the positively charged Pyrgos[*n*]cages interacted with the bacterial membrane (*45*). Consistent

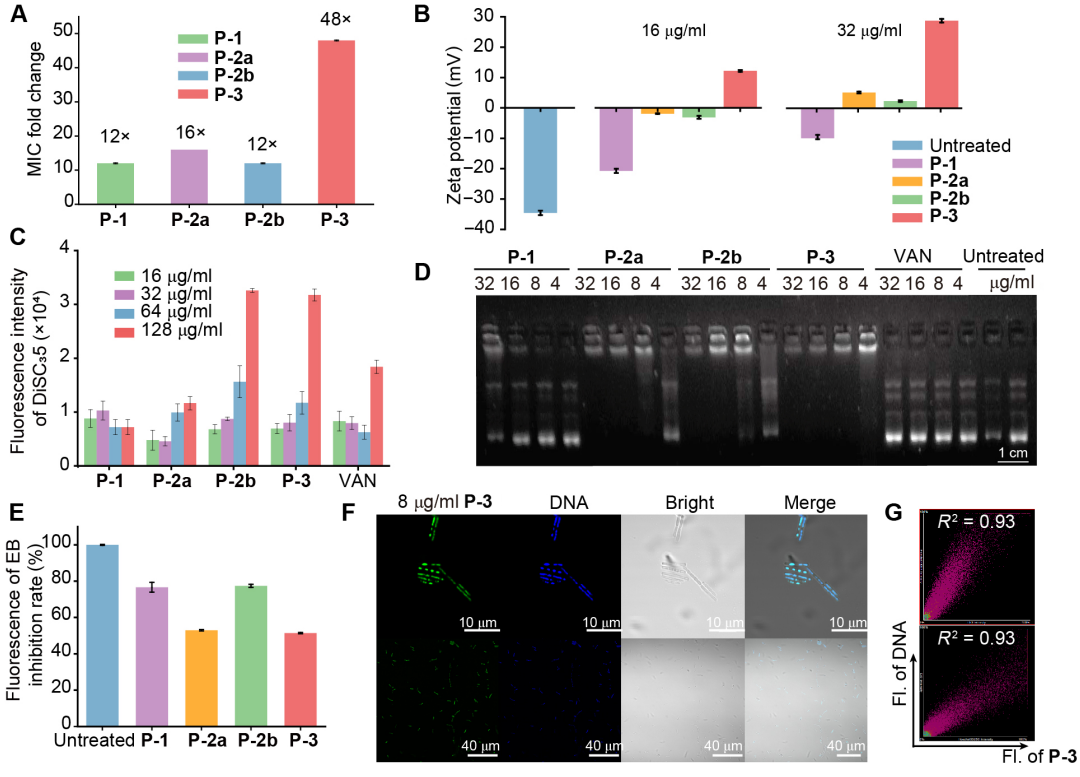

Fig. 5. Membrane-targeting activity assays and DNA-targeting activity assays. (**A**) The exogenous PG interference assay suggested that Pyrgos[*n*]cages have an interaction with PG, especially. (**B**) Zeta potential changes of bacteria after being treated with Pyrgos[*n*]cages of different concentrations (16 and 32 μg/ml). (**C**) Results from the cytoplasmic membrane depolarization assay. Apparent cell membrane disruption by addition of Pyrgos[*n*]cages could be observed. (**D**) Gel retardation assay showing the complexation of a 6500–base pair plasmid DNA (Pcold-ctxm-15) and Pyrgos[*n*]cages/vancomycin (VAN). DNA was fluorescently labeled by Gel-Red, an intercalator-type dye. (**E**) Upon the introduction of 64 mM of the compound, we observed a remarkable inhibition of EB-DNA fluorescence, indicating the compound's potential to interact with and perturb the structure. This observation has been well documented and is presented in the accompanying experimental data. (**F**) Confocal microscopic images showing **P-3**-stained bacteria cells and DNA stained by 4′,6-diamidino-2-phenylindole (DAPI) in *B. subtilis* [blue: DAPI-stained *B. subtilis* DNA, excitation (Ex) = 405 nm, emission (Em) = 425 to 475 nm; green: **P-3** fluorescence, Ex = 405 nm, Em = 500 to 550 nm). Scale bars, 10 and 40 μm. (**G**) The two-dimensional (2D) intensity histogram was plotted using **P-3** fluorescence and DAPI fluorescence against nucleus fluorescence, respectively.

with the results of lipid interference assays, **P-3**, the molecule with the most deckers, exhibited the most prominent effect on surface potential change.

Following the demonstrated membrane interaction of Pyrgos[*n*] cages, we proceeded to examine their impact on the structural integrity and functions of bacterial membranes, including the permeability barrier and bioenergetic transduction sites. Traditionally, AMPs are recognized for seriously disrupting bacterial membrane structures through mechanisms such as toroidal pore formation, barrel-stave pore formation, or carpet-like disruption. These actions result in severe deformation of membrane integrity and the leakage of cellular contents (*46*). To investigate the impact of Pyrgos[*n*]cages on bacterial membrane structure, we initially observed the morphology of *S. aureus* cells treated with **P-3** and noted no substantial membrane rupture (fig. S50). Similarly, using the propidium iodide membrane permeability assay, we detected no substantial alteration in membrane permeability following the treatment with Pyrgos[*n*] cages (fig. S51). These findings collectively indicated that Pyrgos[*n*] cages, unlike traditional AMPs, may affect the bacterial cell membrane less destructively. The observed antimicrobial activity could therefore stem from interference with critical membrane functions, such as bioenergetic transduction.

To test our hypothesis regarding membrane potential changes, which are critical for a broad spectrum of bacterial physiological processes and behaviors (*47*) including antibiotic resistance (*48*), cell division (*49*), and environmental sensing (*50*), we conducted cytoplasmic membrane depolarization assays using a $DiSC_35$ dye. This potentiometric probe accumulates on hyperpolarized membranes and integrates into the lipid bilayer, where its fluorescence is quenched at high concentrations. Thus, an increase in $DiSC_35$ fluorescence signals membrane potential dissipation. Our results, depicted in Fig. 5C, demonstrated that Pyrgos[*n*]cage treatment elevated fluorescence intensity, signifying membrane potential disruption. Furthermore, **P-3** would interact with bacterial cell surfaces through electrostatic attraction, a process that can lead to the aggregation of bacteria into clusters. This aggregation creates a microenvironment where the diffusion of nutrients and signaling molecules is heavily compromised, potentially altering the metabolic and communicative processes of the bacteria (figs. S52 and S53) (*51*–*53*). Notably, **P-3** exhibited the most substantial depolarizing effect, followed by **P-2b**, **P-2a**, and **P-1**, aligning with their lipid-binding affinity and surface attachment capabilities as shown in Fig. 5, A and B.

Beyond disrupting bacterial membrane, some natural AMPs can penetrate bacterial membranes to inhibit additional intracellular bacterial targets (*54*, *55*). Given the cationic structure of Pyrgos[*n*] cages and their membrane-associating activity, it is plausible that they might internalize within cells to act against intracellular targets such as negatively charged DNA. In vitro gel retardation assays indicated a dose-dependent DNA migration retardation with Pyrgos[*n*] cages addition (Fig. 5D). Furthermore, a fluorophotometric competition assay revealed that **P-3** is the most potent DNA binder among Pyrgos[*n*]cages, as evidenced by its ability to displace the known DNA binder ethidium bromide (EB), resulting in fluorescence loss (Fig. 5E and figs. S54 and S55). This enhanced binding capacity may be due to increased multivalent interactions as the number of cage layers rises. Using molecular operating environment for molecular docking, the results (fig. S56) indicate that the most probable DNA binding mode is a groove binding mode. This interaction involved the observation of hydrophobic interactions, hydrogen bonds, and π-π stacking involving arene C─H bonds. We also explored **P-3**'s potential for cellular internalization and subsequent DNA binding. Confocal microscopy demonstrated marked colocalization of **P-3**'s green fluorescence with Hoechst, a DNA-specific dye permeable to bacteria (Fig. 5F), with a colocalization coefficient of 0.93 (Fig. 5G and fig. S57), suggesting successful internalization and DNA interaction.

Together, the interactions with biomacromolecules indicated that Pyrgos[*n*]cages, particularly **P-3**, diverge from classical AMPs by not solely disrupting membrane integrity. Instead, they exert antimicrobial effects by embedding into the bacterial membrane and further permeating into the cell to target intracellular DNA. This distinctive dual-targeting approach not only underpins the potent antibacterial activity of **P-3** but also ensures the biocompatibility necessary for practical applications in ex vivo and in vivo disease-related studies, which are explored in the subsequent section.

Eradication of intracellular *S. aureus* by Pyrgos[*n*]cages with notable biocompatibility

On the basis of in vitro antibacterial activity and antimicrobial resistance, we further investigated the antimicrobial effect of Pyrgos[*n*] cages under more physiologically related bacterial infection conditions, especially with the consideration of *S. aureus* being a stubborn intracellular persisting pathogen. Accumulating evidence suggests that *S. aureus* can adapt to an intracellular lifestyle in various host cells including keratinocytes, endothelial cells, epithelial cells, fibroblast, osteoblasts, and macrophages, contributing to chronic infections and antibiotic resistance (*4*, *12*). After being phagocytosed, *S. aureus* resides in early phagosomes, advances to late phagosomes, and ultimately merges with lysosomes to form phagolysosomes (Fig. 6A). Within the acidic phagolysosome environment, *S. aureus* assumes a dormant persister cell state, acting as a reservoir for recurrent infections. Therefore, these distinct microbiological traits suggest that, for Pyrgos[*n*]cages to be effective in combatting intracellular *S. aureus*, three preliminary requirements have to be fulfilled: (i) antimicrobial activity against the dormant persistent intracellular style of *S. aureus*, (ii) sufficient uptake within *S. aureus*–infected cells, and (iii) precise colocalization with the *S. aureus*–residing phagolysosomes.

Activity against dormant *S. aureus* cells was demonstrated with an artificial slow-growth culturing condition with phosphate-buffered saline (PBS) (*56*). As shown in Fig. 6B, while conventional antibiotic vancomycin fails to kill dormant *S. aureus* with a concentration up to 8 μg/ml, **P-3** effectively eradicated these persisting bacteria at 0.25 μg/ml, a dose comparable to its activity against active growth *S. aureus*. Consistent results were obtained with a higher initial inoculum of bacteria (fig. S58). Next, intracellular uptake of Pyrgos[*n*]cages was quantified by flow cytometry, indicating a remarkable level of accumulation of these molecules (Fig. 6C). The intracellular localization of **P-3** in *S. aureus*–infected macrophages (Sa@RAW) was then examined using high-resolution confocal microscopy. The results revealed a pronounced cocolonization between **P-3** and *S. aureus* (Fig. 6D-i and fig. S59A), with a colonization coefficient of 0.73. Further investigation suggested that this favorable drug-bacteria cocolonization may stem from the phagosomal localization of *S. aureus* (Fig. 6D-ii and fig. S59B) and the lysosomal localization of **P-3** (Fig. 6D-iii and fig. S59C). Drug-bacteria cocolonization was thus facilitated by the subsequent fusion of the *S. aureus*–containing phagosome and **P-3**–containing

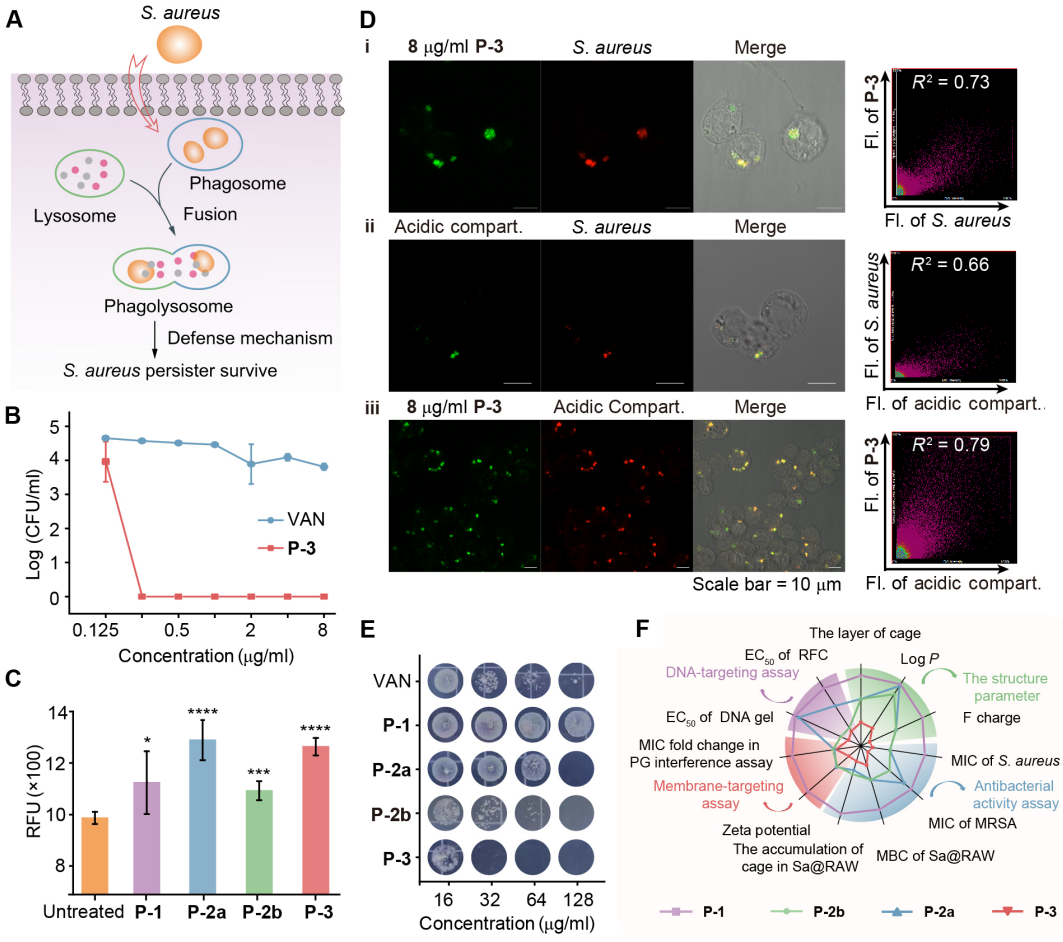

Fig. 6. Intracellular antimicrobial activities of Pyrgos[*n*]cages and colocalization with the *S. aureus*–residing phagolysosomes. (**A**) Phagocytosis of *S. aureus* and the phagosome-lysosome fusion event. (**B**) Killing effect of dormant 5×10^5 colony-forming units (CFU) of *S. aureus* in the presence of **P-3** and vancomycin. (**C**) The accumulation of Pyrgos[*n*]cages in Sa@RAW after 4 hours treated by Pyrgos[*n*]cages (8 μg/ml). RFU, relative fluorescence unit. (**D**) Illustration of the intracellular localization of **P-3** and phagocytosed *S. aureus* and confocal microscopic images of Sa@RAW. Subcellular colocalization of (i) **P-3** and *S. aureus* (green: **P-3** fluorescence, Ex = 405 nm, Em = 500 to 550 nm; red: EB-stained *S. aureus*, Ex = 561 nm, Em =570 to 620 nm); (ii) Sa@RAW suggesting the residence of *S. aureus* in the acidic mycobacteria pathogen vacuoles (pH ~ 6.2) (green: lysotracker-green to stain acidic compartments, Ex = 488 nm, Em = 500 to 550 nm; red: EB-stained, Ex = 561 nm, Em =570 to 620 nm); (iii) **P-3**, suggesting the residence of **P-3** in the acidic endosomes or lysosomes (green: **P-3** fluorescence, Ex = 405 nm, Em = 500 to 550 nm; red: lysotracker-red to stain acidic compartments, Ex = 561 nm, Em =570 to 620 nm) is shown. The 2D intensity histogram was plotted using (i) **P-3** fluorescence and EB fluorescence against *S. aureus*; (ii) lysotracker-green fluorescence against acidic compartments and EB fluorescence against *S. aureus*; (iii) **P-3** fluorescence and lysotracker-red fluorescence against acidic compartments, respectively. (**E**) Minimum bactericidal concentration (MBC) of compounds against Sa@RAW, with or without Pyrgos[*n*]cages of interest Dulbecco's modified Eagle's medium supplemented with 10% fetal bovine serum after requiring 24 hours. (**F**) Multiparameter radar chart presenting the correlation between antimicrobial activity, membrane-targeting activity, DNA-targeting activity, and the structure parameter. EC_{50}, median effective concentration

lysosome, forming phagolysosomes, in line with the natural intracellular fate of *S. aureus*.

The efficacy against dormant persistent bacteria, coupled with sufficient accumulation and precise colocalization within the phagolysosome compartment, underscores the activity of **P-3** against challenging intracellular *S. aureus*, with noticeable improvement over the conventional antibiotic vancomycin (Fig. 6E). Note that **P-3** displays the highest level of activity among the Pyrgos[*n*]cages, aligning with the effects on biomacromolecule targeting. Inspired by this correlation, we further reviewed the relationship between the multidecker chemical structure of Pyrgos[*n*]cages, biomacromolecular binding affinity, and their antibacterial activities (Fig. 6F). Increasing the number of deckers brings together increased positive charge (F charge) and hydrophobicity (log *P*) in the Pyrgos[*n*]cages series, facilitating the interactions of **P-3** with biomacromolecules in a multivalent manner. The cooperative nature of such multivalency, together with the dual-targeting mechanism of action, thus results in the most potent in vitro and in cellular antimicrobial activities of **P-3**. Together with its demonstrated cellular biocompatibility, **P-3** represents a promising antimicrobial agent for subsequent in vivo study with an *S. aureus*–infected animal model.

In vivo antimicrobial activities of Pyrgos[*n*]cages in a *S. aureus* skin infection model

Wound infections affecting the dermis, including burns, surgical site infections, and diabetic foot ulcers, pose substantial challenges in health care (*57*). Recognizing that *S. aureus* is a prevalent contributor to chronic wound infections (*58*, *59*), we established a

mouse excision wound model infected with *S. aureus* to assess the efficacy of **P-3**. In this model study, large surface wounds were artificially created on mice, and the wound areas were infected with a high load of a highly virulent MRSA (carbapenem-resistant *Acinetobacter baumannii*) clinical isolate (10^8 colony-forming units). The wound area underwent treatment with vancomycin, **P-3**, and PBS over 7 days, with the mice's status observed for an additional 7 days (see flowchart in Fig. 7A). We observed that **P-3** treatment led to enhanced sterilization of the wound surface throughout the entire treatment period (Fig. 7B). After just 1 day of treatment, there was a four-log reduction in bacterial load on the wound surface (Fig. 7C), representing a substantial improvement over the other treatment groups. The Pyrgos[*n*]cages treatment also facilitated wound healing (figs. S60 and S61) with a notably improved recovery of the wound area. As depicted in Fig. 7D, the hematoxylin and eosin (H&E) stain analysis of the wound section in the PBS group reveals a partial loss of the epidermis in the skin tissue (red arrow), accompanied by a locally remarkable thickening of the skin in the affected area (black arrow). In sharp contrast, the wound section of the **P-3** group exhibited intact skin with a moderate level of thickening (black arrow). No toxicity was observed during the **P-3** treatment, as indicated by both the mouse body weight change (Fig. 7E) and the immunohistogram of major organs after treatment (Fig. 7F). Collectively, the in vivo data suggested that **P-3**, endowed with an antiresistant mechanism of action stemming from a new chemical molecular design, holds promise for the treatment of the notorious *S. aureus* skin infection.

DISCUSSION

In conclusion, we unveil a series of Pyrgos[*n*]cage-ingeniously engineered multidecker cationic covalent organic cage–achieved through innovative photocatalytic bromination and precise cage-forming reactions. These structures, characterized by their ease of synthesis, modifiable dimensions, exceptional rigidity, and extraordinary stability, stand out for their densely packed, uniformly distributed positive charges. Demonstrating a remarkable ability for selective interaction with bacterial rather than human cells, Pyrgos[*n*]cages exert potent bactericidal effects by simultaneously targeting bacterial membranes and DNA. A notable specificity for Gram-positive over Gram-negative bacteria was observed, with ex vivo studies revealing that the **P-3** variant eradicated *S. aureus* while preserving mammalian cell integrity. Crucially, in vivo experiments in mouse models infected with methicillin-resistant *S. aureus* showcased **P-3**'s outstanding bactericidal efficacy with minimal toxicity, heralding these molecular frameworks as pivotal advances in combating drug-resistant bacterial infections. This study not only sets a new paradigm in antibacterial strategy but also charts the course for future innovations in antimicrobial therapy. Subsequent efforts will aim to broaden the antimicrobial

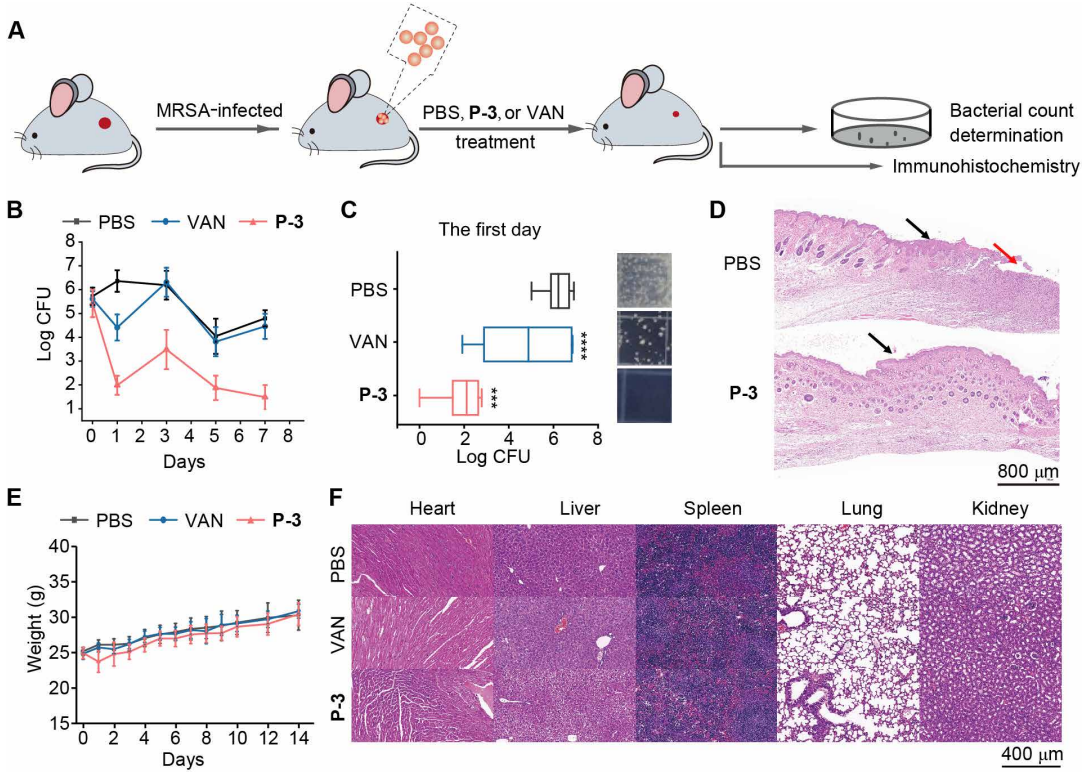

Fig. 7. In vivo antimicrobial activities of P-3 in a *S. aureus* skin infection model. (**A**) Schematic diagram of *S. aureus* cutaneous abscess infection and treated. $N = 6$ for the **P-3** group, $N = 6$ for the vancomycin group, $N = 6$ for the PBS group. (**B**) Comparison of bacterial loads of major organs for PBS, vancomycin, and **P-3** treatment groups. The day after the wound was coated with bacteria was the starting day of counting. (**C**) Quantification of bacteria burden and the bacterial colony images on survived mice's wound areas on first day. (**D**) H&E stain analysis of the wound area of the survived mice at day 8. (**E**) The infected mouse weights change during treatment. (**F**) Organ tissue H&E staining analysis for different treatment groups at day 8.

spectrum of Pyrgos[*n*]cages, particularly against Gram-negative pathogens, by enhancing their affinity for lipopolysaccharides, thus underscoring the transformative potential of covalent organic cages in addressing the urgent challenge of antibiotic resistance.

MATERIALS AND METHODS

All solvents and reagents were purchased from commercial sources without further purification. ^{1}H and ^{13}C nuclear magnetic resonance spectra were collected using Bruker AVANCE 400, and deuterated solvents were purchased from Cambridge Isotope Laboratories. Residual solvent peaks were used as internal reference [$CDCl_3$ δ = 7.26 parts per million (ppm), D_2O δ = 4.79 ppm, CD_3CN δ = 1.94 ppm, and dimethyl sulfoxide–d_6 δ = 2.50 ppm]. High-resolution mass spectrometry (electrospray ionization) was recorded on Bruker Apex-Q IV FTMS mass spectrometer. X-ray crystallographic data were collected on Bruker D8 Venture diffractometer. All the flow cytometry studies were performed on a Becton Dickinson Accuri C6 Plus instrument. Zeta potential was conducted on a Malvern Zetasizer Nano ZSP instrument. Fluorescence spectroscopies were measured on a Hitachi F-7000 fluorescence spectrophotometer. Fluorescence microscope images were acquired using a Nikon Eclipse Ti2-E Laser Confocal Microscope. For blue/cyan fluorescence, wavelength was set at 405 nm for excitation. For green fluorescence, wavelength was set at 488 nm for excitation. For red fluorescence, wavelength was set at 561 nm for excitation. The part of obtained data was processed through Origin 2017 and GraphPad Prism 8 and then saved as vector image files (*.eps) for coloring and annotation in Adobe Illustrator CC 2015.

Water was obtained from a Milli-Q purification system. The following bacteria were purchased from the American Type Culture Collection (ATCC, Manassas, VA): *S. aureus* Newman strain (ATCC, 25904), *S. aureus* USA300 (ATCC, BAA-1717), *B. subtilis* from subsp. *subtilis* (Ehrenberg) Cohn (ATCC, 6051), *Enterococcus faecalis* (Andrewes and Horder) Schleifer and Kilpper-Balz (ATCC, 19433), *Klebsiella pneumoniae* subsp. *pneumoniae* Schroeter Trevisan (ATCC, 27736), *A. baumannii* Bouvet and Grimont (ATCC, 19606), *Pseudomonas aeruginosa* PA01 (ATCC, 47085), and *E. coli* K12 (ATCC 29425) was from TsingKe Biological Technology, Beijing. *P. aeruginosa* reference strain 14 was obtained from BEI Resources. Bacterial clinical isolates were from Shenzhen People's Hospital and Peking University People's Hospital. All bacteria strains were confirmed by 16*S* ribosomal DNA sequencing. *Homo sapiens* embryonic kidney cell line human embryonic kidney (HEK) 293 (ATCC, CRL-3216) and murine macrophage cell line RAW 264.7 (ATCC, TIB71) were purchased from ATCC. Bacteria names without an affix or note are laboratory strains.

Supplementary Materials

The PDF file includes:

Figs. S1 to S64
Tables S1 to S4
Legend for data S1
References

Other Supplementary Material for this manuscript includes the following:

Data S1

REFERENCES AND NOTES

1. D. M. P. De Oliveira, B. M. Forde, T. J. Kidd, P. N. A. Harris, M. A. Schembri, S. A. Beatson, D. L. Paterson, M. J. Walker, Antimicrobial resistance in ESKAPE pathogens. *Clin. Microbiol. Rev.* **33**, e00181-19 (2020).
2. E. D. Brown, G. D. Wright, Antibacterial drug discovery in the resistance era. *Nature* **529**, 336–343 (2016).
3. L. L. Silver, Challenges of antibacterial discovery. *Clin. Microbiol. Rev.* **24**, 71–109 (2011).
4. E. Oldfield, X. Feng, Resistance-resistant antibiotics. *Trends Pharmacol. Sci.* **35**, 664–674 (2014).
5. S. Bai, J. Wang, K. Yang, C. Zhou, Y. Xu, J. Song, Y. Gu, Z. Chen, M. Wang, C. Shoen, B. Andrade, M. Cynamon, K. Zhou, H. Wang, Q. Cai, E. Oldfield, S. C. Zimmerman, Y. Bai, X. Feng, A polymeric approach toward resistance-resistant antimicrobial agent with dual-selective mechanisms of action. *Sci. Adv.* **7**, eabc9917 (2021).
6. M. Miethke, M. Pieroni, T. Weber, M. Brönstrup, P. Hammann, L. Halby, P. B. Arimondo, P. Glaser, B. Aigle, H. B. Bode, R. Moreira, Y. Li, A. Luzhetskyy, M. H. Medema, J.-L. Pernodet, M. Stadler, J. R. Tormo, O. Genilloud, A. W. Truman, K. J. Weissman, E. Takano, S. Sabatini, E. Stegmann, H. Brötz-Oesterhelt, W. Wohlleben, M. Seemann, M. Empting, A. K. H. Hirsch, B. Loretz, C.-M. Lehr, A. Titz, J. Herrmann, T. Jaeger, S. Alt, T. Hesterkamp, M. Winterhalter, A. Schiefer, K. Pfarr, A. Hoerauf, H. Graz, M. Graz, M. Lindvall, S. Ramurthy, A. Karlén, M. van Dongen, H. Petkovic, A. Keller, F. Peyrane, S. Donadio, L. Fraisse, L. J. V. Piddock, I. H. Gilbert, H. E. Moser, R. Müller, Towards the sustainable discovery and development of new antibiotics. *Nat. Rev. Chem.* **5**, 726–749 (2021).
7. A. G. Atanasov, S. B. Zotchev, V. M. Dirsch; International Natural Product Sciences Taskforce, C. T. Supuran, Natural products in drug discovery: Advances and opportunities. *Nat. Rev. Drug Discov.* **20**, 200–216 (2021).
8. S. Lin, J. D. Wade, S. Liu, De novo design of flavonoid-based mimetics of cationic antimicrobial peptides: Discovery, development, and applications. *Acc. Chem. Res.* **54**, 104–119 (2021).
9. E. M. Darby, E. Trampari, P. Siasat, M. S. Gaya, I. Alav, M. A. Webber, J. M. A. Blair, Molecular mechanisms of antibiotic resistance revisited. *Nat. Rev. Microbiol.* **21**, 280–295 (2023).
10. C. Walsh, Molecular mechanisms that confer antibacterial drug resistance. *Nature* **406**, 775–781 (2000).
11. W. P. J. Smith, B. R. Wucher, C. D. Nadell, K. R. Foster, Bacterial defences: Mechanisms, evolution and antimicrobial resistance. *Nat. Rev. Microbiol.* **21**, 519–534 (2023).
12. L. L. Silver, Multi-targeting by monotherapeutic antibacterials. *Nat. Rev. Drug Discov.* **6**, 41–55 (2007).
13. J. G. Hurdle, A. J. O'Neill, I. Chopra, R. E. Lee, Targeting bacterial membrane function: An underexploited mechanism for treating persistent infections. *Nat. Rev. Microbiol.* **9**, 62–75 (2011).
14. N. C. Rosas, T. Lithgow, Targeting bacterial outer-membrane remodelling to impact antimicrobial drug resistance. *Trends Microbiol.* **30**, 544–552 (2022).
15. X. Chen, F. Niyonsaba, H. Ushio, D. Okuda, I. Nagaoka, S. Ikeda, K. Okumura, H. Ogawa, Synergistic effect of antibacterial agents human β-defensins, cathelicidin LL-37 and lysozyme against *Staphylococcus aureus* and *Escherichia coli*. *J. Dermatol. Sci.* **40**, 123–132 (2005).
16. N. Chen, C. Jiang, Antimicrobial peptides: Structure, mechanism, and modification. *Eur. J. Med. Chem.* **255**, 115377 (2023).
17. J. Svenson, N. Molchanova, C. I. Schroeder, Antimicrobial peptide mimics for clinical use: Does size matter? *Front. Immunol.* **13**, 915368 (2022).
18. S. Xu, P. Tan, Q. Tang, T. Wang, Y. Ding, H. Fu, Y. Zhang, C. Zhou, M. Song, Q. Tang, Z. Sun, X. Ma, Enhancing the stability of antimicrobial peptides: From design strategies to applications. *Chem. Eng. J.* **475**, 145923 (2023).
19. A. Hollmann, M. Martinez, P. Maturana, L. C. Semorile, P. C. Maffia, Antimicrobial peptides: Interaction with model and biological membranes and synergism with chemical antibiotics. *Front. Chem.* **6**, 204 (2018).
20. C. D. Fjell, J. A. Hiss, R. E. W. Hancock, G. Schneider, Designing antimicrobial peptides: Form follows function. *Nat. Rev. Drug Discov.* **11**, 37–51 (2012).
21. R. Mourtada, H. D. Herce, D. J. Yin, J. A. Moroco, T. E. Wales, J. R. Engen, L. D. Walensky, Design of stapled antimicrobial peptides that are stable, nontoxic and kill antibiotic-resistant bacteria in mice. *Nat. Biotechnol.* **37**, 1186–1197 (2019).
22. C. Guo, Y. Tu, Q. Zhang, Y. Jiang, Y. Ding, S. Xiao, L. Tan, Engineering magnetically induced antibacterial organic/inorganic hybrid nanoparticles for the treatment of periodontitis. *Giant* **13**, 100145 (2023).
23. Z. Meng, L. Pan, S. Qian, X. Yang, L. Pan, R. Chi, J. Chen, J. Pan, C. Shi, Antimicrobial peptide nanoparticles coated with macrophage cell membrane for targeted antimicrobial therapy of sepsis. *Mater. Des.* **229**, 111883 (2023).
24. X. Gu, Z. Xu, L. Gu, H. Xu, F. Han, B. Chen, X. Pan, Preparation and antibacterial properties of gold nanoparticles: A review. *Environ. Chem. Lett.* **19**, 167–187 (2021).
25. L. Gao, H. Wang, B. Zheng, F. Huang, Combating antibiotic resistance: Current strategies for the discovery of novel antibacterial materials based on macrocycle supramolecular chemistry. *Giant* **7**, 100066 (2021).
26. S. Guo, Y. He, Y. Zhu, Y. Tang, B. Yu, Combatting antibiotic resistance using supramolecular assemblies. *Pharmaceuticals* **15**, 804 (2022).
27. X. Li, H. Bai, Y. Yang, J. Yoon, S. Wang, X. Zhang, Supramolecular antibacterial materials for combatting antibiotic resistance. *Adv. Mater.* **31**, e1805092 (2019).
28. Z. Y. Zhang, C. Li, Biphen[*n*]arenes: Modular synthesis, customizable cavity sizes, and diverse skeletons. *Acc. Chem. Res.* **55**, 916–929 (2022).

29. L. Xia, J. Tian, T. Yue, H. Cao, J. Chu, H. Cai, W. Zhang, Pillar[5]arene-based acid-triggered supramolecular porphyrin photosensitizer for combating bacterial infections and biofilm dispersion. *Adv. Healthc. Mater.* **11**, e2102015 (2022).
30. S. Guo, Q. Huang, Y. Chen, J. Wei, J. Zheng, L. Wang, Y. Wang, R. Wang, Synthesis and bioactivity of guanidinium-functionalized pillar[5]arene as a biofilm disruptor. *Angew. Chem. Int. Ed. Engl.* **60**, 618–623 (2020).
31. D. N. Shurpik, P. L. Padnya, I. I. Stoikov, P. J. Cragg, Antimicrobial activity of calixarenes and related macrocycles. *Molecules* **25**, 5145 (2020).
32. M. Mourer, J. B. Regnouf-de-Vains, R. E. Duval, Functionalized calixarenes as promising antibacterial drugs to face antimicrobial resistance. *Molecules* **28**, 6954 (2023).
33. B. Hu, C. Owh, P. L. Chee, W. R. Leow, X. Liu, Y.-L. Wu, P. Guo, X. J. Loh, X. Chen, Supramolecular hydrogels for antimicrobial therapy. *Chem. Soc. Rev.* **47**, 6917–6929 (2018).
34. Z. Huang, H. Zhang, H. Bai, Y. Bai, S. Wang, X. Zhang, Polypseudorotaxane constructed from cationic polymer with cucurbit[7]uril for controlled antibacterial activity. *ACS Macro Lett.* **5**, 1109–1113 (2016).
35. L. Gao, M. Li, S. Ehrmann, Z. Tu, R. Haag, Positively charged nanoaggregates based on zwitterionic pillar[5]arene that combat planktonic bacteria and disrupt biofilms. *Angew. Chem. Int. Ed. Engl.* **58**, 3645–3649 (2019).
36. J.-J. Li, Y. Hu, B. Hu, W. Wang, H. Xu, X.-Y. Hu, F. Ding, H.-B. Li, K.-R. Wang, X. Zhang, D.-S. Guo, Lactose azocalixarene drug delivery system for the treatment of multidrug-resistant pseudomonas aeruginosa infected diabetic ulcer. *Nat. Commun.* **13**, 6279 (2022).
37. P. G. Lima, J. T. A. Oliveira, J. L. Amaral, C. D. T. Freitas, P. F. N. Souza, Synthetic antimicrobial peptides: Characteristics, design, and potential as alternative molecules to overcome microbial resistance. *Life Sci.* **278**, 119647 (2021).
38. G. Montà-González, F. Sancenón, R. Martínez-Máñez, V. Martí-Centelles, Purely covalent molecular cages and containers for guest encapsulation. *Chem. Rev.* **122**, 13636–13708 (2022).
39. A. Li, S. Xiong, W. Zhou, H. Zhai, Y. Liu, Q. He, Superphane: A new lantern-like receptor for encapsulation of a water dimer. *Chem. Commun.* **57**, 4496–4499 (2021).
40. A. Li, Y. Liu, W. Zhou, Y. Jiang, Q. He, Superphanes: Facile and efficient preparation, functionalization and unique properties. *Tetrahedron Chem* **1**, 100006 (2022).
41. W. Zhou, F. Wang, A. Li, S. Bai, X. Feng, Q. He, A superphane-based carcer and for arsenic detoxification via imprisoning arsenate. *Cell Rep. Phys. Sci.* **4**, 101295 (2023).
42. W. Zhou, A. Li, M. Zhou, Y. Xu, Y. Zhang, Q. He, Nonporous amorphous superadsorbents for highly effective and selective adsorption of iodine in water. *Nat. Commun.* **14**, 5388 (2023).
43. N. A. Turner, B. K. Sharma-Kuinkel, S. A. Maskarinec, E. M. Eichenberger, P. P. Shah, M. Carugati, T. L. Holland, V. G. Fowler Jr., Methicillin-resistant *Staphylococcus aureus*: An overview of basic and clinical research. *Nat. Rev. Microbiol.* **17**, 203–218 (2019).
44. F. Liu, X. Zhang, X. Xiao, Q. Duan, H. Bai, Y. Cao, Y. Zhang, M. Alee, L. Yu, Improved hydrophobicity, antibacterial and mechanical properties of polyvinyl alcohol/quaternary chitosan composite films for antibacterial packaging. *Carbohydr. Polym.* **312**, 120755 (2023).
45. C. Gao, C. H. T. Kwong, M. Tang, J. Liu, H. Kam, S. Li, S. M. Y. Lee, C. Fan, H.-Z. Yu, R. Wang, A bacterially engineered macrophage sponge as a neutralization decoy to treat bacterial infection. *Matter* **6**, 3889–3911 (2023).
46. K. A. Brogden, Antimicrobial peptides: Pore formers or metabolic inhibitors in bacteria? *Nat. Rev. Microbiol.* **3**, 238–250 (2005).
47. J. M. Benarroch, M. Asally, The microbiologist's guide to membrane potential dynamics. *Trends Microbiol.* **28**, 304–314 (2020).
48. P. D. Damper, W. Epstein, Role of the membrane potential in bacterial resistance to aminoglycoside antibiotics. *Antimicrob. Agents Chemother.* **20**, 803–808 (1981).
49. H. Strahl, L. W. Hamoen, Membrane potential is important for bacterial cell division. *Proc. Natl. Acad. Sci. U.S.A.* **107**, 12281–12286 (2010).
50. G. N. Bruni, R. A. Weekley, B. J. T. Dodd, J. M. Kralj, Voltage-gated calcium flux mediates *Escherichia coli* mechanosensation. *Proc. Natl. Acad. Sci. U.S.A.* **114**, 9445–9450 (2017).
51. L. T. Lui, X. Xue, C. Sui, A. Brown, D. I. Pritchard, N. Halliday, K. Winzer, S. M. Howdle, F. Fernandez-Trillo, N. Krasnogor, C. Alexander, Bacteria clustering by polymers induces the expression of quorum-sensing-controlled phenotypes. *Nat. Chem.* **5**, 1058–1065 (2013).
52. D.-W. Lee, T. Kim, I.-S. Park, Z. Huang, M. Lee, Multivalent nanofibers of a controlled length: Regulation of bacterial cell agglutination. *J. Am. Chem. Soc.* **134**, 14722–14725 (2012).
53. G. Pasparakis, A. Cockayne, C. Alexander, Control of bacterial aggregation by thermoresponsive glycopolymers. *J. Am. Chem. Soc.* **129**, 11014–11015 (2007).
54. S. Li, Y. Wang, Z. Xue, Y. Jia, R. Li, C. He, H. Chen, The structure-mechanism relationship and mode of actions of antimicrobial peptides: A review. *Trends Food Sci. Technol.* **109**, 103–115 (2021).
55. Q.-Y. Zhang, Z.-B. Yan, Y.-M. Meng, X.-Y. Hong, G. Shao, J.-J. Ma, X.-R. Cheng, J. Liu, J. Kang, C.-Y. Fu, Antimicrobial peptides: Mechanism of action, activity and clinical potential. *Mil. Med. Res.* **8**, 48 (2021).
56. S. Mukherjee, S. Barman, R. Mukherjee, J. Haldar, Amphiphilic cationic macromolecules highly effective against multi-drug resistant Gram-positive bacteria and fungi with no detectable resistance. *Front. Bioeng. Biotechnol.* **8**, 55 (2020).
57. R. D. Wolcott, D. D. Rhoads, M. E. Bennett, B. M. Wolcott, L. Gogokhia, J. W. Costerton, S. E. Dowd, Chronic wounds and the medical biofilm paradigm. *J. Wound Care* **19**, 45–53 (2010).
58. S. DeLeon, A. Clinton, H. Fowler, J. Everett, A. R. Horswill, K. P. Rumbaugh, Synergistic interactions of *Pseudomonas aeruginosa* and *Staphylococcus aureus* in an in vitro wound model. *Infect. Immun.* **82**, 4718–4728 (2014).
59. M. Fazli, T. Bjarnsholt, K. Kirketerp-Møller, B. Jørgensen, A. S. Andersen, K. A. Krogfelt, M. Givskov, T. Tolker-Nielsen, Nonrandom distribution of *Pseudomonas aeruginosa* and *Staphylococcus aureus* in chronic wounds. *J. Clin. Microbiol.* **47**, 4084–4089 (2009).
60. J. Závada, M. Pánková, P. Holý, M. Tichý, A facile synthesis of hexakis(bromomethyl) benzene from mesitylene. *Synthesis* , 1132 (1994).
61. S. N. L. Andree, A. S. Sinha, C. B. Aakeröy, Structural examination of halogen-bonded co-crystals of tritopic acceptors. *Molecules* **23**, 163 (2018).
62. Y. Yuan, Z.-L. Jiang, J.-M. Yan, G. Gao, A. S. C. Chan, R.-G. Xie, A convenient and effective synthesis of tris-bridged tricationic azolophanes. *Synth. Commun.* **30**, 4555–4561 (2007).
63. O. V. Dolomanov, L. J. Bourhis, R. J. Gildea, J. A. K. Howard, H. Puschmann, OLEX2: A complete structure solution, refinement and analysis program. *J. Appl. Cryst.* **42**, 339–341 (2009).
64. G. M. Sheldrick, *SHELXT*–Integrated space-group and crystal-structure determination. *Acta Crystallogr. A Found. Adv.* **71**, 3–8 (2015).
65. G. M. Sheldrick, Crystal structure refinement with *SHELXL*. *Acta Crystallogr. C Struct. Chem.* **71**, 3–8 (2015).

Acknowledgments: We acknowledge the technical support of standard spectroscopic analysis (e.g., nuclear magnetic resonance and high-resolution mass spectrometry) at Analytical Instrumentation Center of Hunan University. We thank Z. Zhang from Bruker (Beijing) Scientific Technology Co., Ltd for helpful discussions on x-ray crystallography. We also sincerely thank H. Yang (Xuzhou Key Laboratory of Laboratory Diagnostics, School of Medical Technology) for providing bacterial strains. **Funding:** This research was funded by the National Natural Science Foundation of China (22071050 and 22371068 to Q. H. and 22177031 to X.F.), National Key Research and Development Program of China (2023YFD1800100 to X.F.), the Natural Science Foundation of Hunan Province (2024JJ4007 to X.F.), Fundamental Research Funds for the Central Universities (Startup Funds to Q. H.), and the Health and Medical Research Fund (HMRF; project no. 22210412 to W.-L.W.), Hong Kong SAR. **Author contributions:** Conceptualization and supervision: Q.H. and X.F. Synthesis and structural characterization: Y.Z. and X.S. Single-crystal growing, data collection, and analysis: Y.Z., W.Z., A.L., and Q.H. Biological experiments and data analysis: M.L. and X.F. Antimicrobial testing for clinical bacterial strains: Y.Y. and H.W. Fund acquisition: Q.H., X.F., and W.-L.W. Writing—original draft: Y.Z., M.L., and X.S. Reviewing and editing: Q.H., X.F., and W.L.W. All authors proofread, commented on, and approved the final version of this manuscript. **Competing interests:** The authors declare that they have no competing interests. **Data and materials availability:** All data needed to evaluate the conclusions in the paper are present in the paper and/or the Supplementary Materials. X-ray structural data for **P-2b**, **P-3**, and **P-4** have been deposited at the Cambridge Crystallographic Data Center under deposition numbers CCDC 2272285, 2270664, and 2270662. Copies of the data can be obtained free of charge via http://www.ccdc.cam.ac.uk/structures/.

Submitted 27 March 2024
Accepted 24 June 2024
Published 26 July 2024
10.1126/sciadv.adp4872